Monthly Notices of the ROYAL ASTRONOMICAL SOCIETY

MNRAS **446,** 2659–2672 (2015) doi:10.1093/mnras/stu2298

Supernova dust formation and the grain growth in the early universe: the critical metallicity for low-mass star formation

Gen Chiaki,[1★] Stefania Marassi,[2] Takaya Nozawa,[3] Naoki Yoshida,[1,4] Raffaella Schneider,[2] Kazuyuki Omukai,[5] Marco Limongi[2,4,6] and Alessandro Chieffi[7]

[1]*Department of Physics, Graduate School of Science, University of Tokyo, 7-3-1 Hongo, Bunkyo, Tokyo 113-0033, Japan*
[2]*INAF/Osservatorio Astronomico di Roma, via Frascati 33, I-00040 Roma, Italy*
[3]*National Astronomical Observatory of Japan, Mitaka, Tokyo 181-8588, Japan*
[4]*Kavli Institute for the Physics and Mathematics of the Universe (WPI), Todai Institutes for Advanced Study, The University of Tokyo, Kashiwa, Chiba 277-8583, Japan*
[5]*Astronomical Institute, Tohoku University, 6-3 Aramaki, Aoba, Sendai 980-8578, Japan*
[6]*European Southern Observatory, Karl-Schwarzschild-Str. 2, D-85748 Garching bei Munchen, Germany*
[7]*INAF/IASF, Via Fosso del Cavaliere 100, I-00133 Roma, Italy*

Accepted 2014 October 24. Received 2014 October 23; in original form 2014 July 17

ABSTRACT

We investigate the condition for the formation of low-mass second-generation stars in the early Universe. It has been proposed that gas cooling by dust thermal emission can trigger fragmentation of a low-metallicity star-forming gas cloud. In order to determine the critical condition in which dust cooling induces the formation of low-mass stars, we follow the thermal evolution of a collapsing cloud by a one-zone semi-analytic collapse model. Earlier studies assume the dust amount in the local Universe, where all refractory elements are depleted on to grains, and/or assume the constant dust amount during gas collapse. In this paper, we employ the models of dust formation and destruction in early supernovae to derive the realistic dust compositions and size distributions for multiple species as the initial conditions of our collapse calculations. We also follow accretion of heavy elements in the gas phase on to dust grains, i.e. grain growth, during gas contraction. We find that grain growth well alters the fragmentation property of the clouds. The critical conditions can be written by the gas metallicity $Z_{\rm cr}$ and the initial depletion efficiency $f_{\rm dep,0}$ of gas-phase metal on to grains, or dust-to-metal mass ratio, as $(Z_{\rm cr}/10^{-5.5}\,{\rm Z}_{\odot}) = (f_{\rm dep,0}/0.18)^{-0.44}$ with small scatters in the range of $Z_{\rm cr} = [0.06\text{–}3.2] \times 10^{-5}\,{\rm Z}_{\odot}$. We also show that the initial dust composition and size distribution are important to determine $Z_{\rm cr}$.

Key words: stars: formation – stars: low-mass – stars: Population II – ISM: abundances – dust, extinction – galaxies: evolution.

1 INTRODUCTION

The first stars (Population III or Pop III stars) formed in metal-free gas are thought to be predominantly massive with several tens to thousand solar masses (Bromm et al. 2001; Abel, Bryan & Norman 2002; Omukai & Palla 2003; Yoshida et al. 2006; Hosokawa et al. 2011; Susa, Hasegawa & Tominaga 2014; Hirano et al. 2014). This is in stark contrast with the typical mass of the Galactic stars which is less than the solar mass (Kroupa 2002). Therefore, how and when the transition of the typical stellar mass occurred is one of the critical issues for understanding the star-forming history throughout the cosmic time. The long-lived low-mass stars discovered in the Galactic halo may be the fossils of the first low-mass stars.

Recent studies propose that the formation of the first low-mass stars is driven by the fine-structure line cooling by carbon and oxygen (Bromm et al. 2001; Bromm & Loeb 2003; Santoro & Shull 2006; Frebel, Johnson & Bromm 2007; Ji, Frebel & Bromm 2014). However, the gas density at which the fine-structure line cooling can cause fragmentation of star-forming clouds is $n_{\rm H} \sim 10^4\text{–}10^5\ {\rm cm}^{-3}$, where the typical mass of the fragments (comparable to the Jeans mass) is expected to be as large as $\sim 100\ {\rm M}_{\odot}$. It appears that the efficient cooling by fine-structure lines at the low densities cannot be the main mechanism to form Jeans-unstable fragments with small masses. Hence, in order to produce low-mass stars in this scenario, protostars must be formed and ejected from such massive clumps by *N*-body interactions before they grow to high masses (e.g. Ji et al. 2014). Although not entirely impossible, the scenario seems to require rather specific conditions. Intriguingly, other studies argue that the presence of dust grains is essential for the formation

★ E-mail: gen.chiaki@utap.phys.s.u-tokyo.ac.jp

of the first low-mass stars; heat transfer via collisions from gas to dust effectively cools the gas and induces the gravitational instability, to trigger the core fragmentation into small clumps. This occurs at very high gas densities of $n_{\rm H} \sim 10^{12}$–$10^{14}\ {\rm cm}^{-3}$, where the typical mass scale of fragments is in the range of ∼0.01–0.1 $M_{\odot}$ (e.g. Schneider et al. 2003, 2006). Assuming a certain grain size distribution and the dust-to-metal mass ratio (∼0.5) of the local interstellar medium, Omukai et al. (2005) derive the critical metallicity of $Z_{\rm cr} \sim 10^{-5.5}\ Z_{\odot}$, above which the dust cooling can trigger the gas fragmentation.

It is important to note that the conditions for fragmentation of low-metallicity gas clouds depend on the properties of dust grains, such as the size distribution and the composition, which are expected to be different in the early Universe. For example, recent observations of damped Lyman α systems with metallicity $Z \sim 10^{-3}\ Z_{\odot}$ reveal that the mass fraction of dust relative to metal is smaller than the present-day value (Molaro et al. 2000; De Cia et al. 2013). In the local Universe, dust grains are thought to be formed in the stellar wind of asymptotic giant branch stars as well as in the ejecta of supernovae. Subsequent accretion of heavy elements on to dust in molecular clouds also contributes the enhancement of dust mass fraction. The prompt formation path of dust in the early Universe is limited to the Pop III supernovae whose progenitors have short lifetimes (Todini & Ferrara 2001; Nozawa et al. 2003). Newly formed grains in the supernova ejecta are, however, destroyed by sputtering after the reverse shocks penetrate into the ejecta (Bianchi & Schneider 2007; Nozawa et al. 2007, hereafter N07; Silvia, Smith & Shull 2010, 2012). Metals locked up in dust grains are partly returned into the gas phase. Therefore, the mass ratio of grains to gas-phase metals can be significantly small. It is thus important to study the role of dust grains in the first galaxies by employing realistic dust formation models.

Schneider et al. (2012a, hereafter S12) and Schneider et al. (2012b) investigate the fragmentation properties of gas clouds pre-enriched with the grains that are produced by Pop III supernovae. They show that the initial dust-to-gas mass ratio is a key quantity for the fragmentation condition. The dust-induced fragmentation is not triggered if this ratio is significantly reduced by the destruction of dust in the supernova ejecta. The conclusion is drawn under the assumption that the size distribution and dust-to-gas mass ratio never change in the course of cloud collapse. Nozawa, Kozasa & Nomoto (2012) point out that the growth of dust grains due to the accretion of heavy elements can take place and increase the dust-to-gas mass ratio even in very low metallicity gas clouds.

Chiaki, Nozawa & Yoshida (2013) show that the cloud fragmentation can be triggered by the grain growth even if the initial fraction of heavy element condensed into grains is as small as 0.001. When the grain growth is considered, the fragmentation conditions rely on the gas metallicity *and* the initial grain size rather than only on the initial dust-to-gas mass ratio. The estimated critical metallicity is $Z_{\rm cr} \sim 10^{-4.5}\ Z_{\odot}$ for the initial grain radii $r_0 \geq 0.1\ \mu$m, and $Z_{\rm cr} \sim 10^{-5.5}\ Z_{\odot}$ for $r_0 \leq 0.01\ \mu$m. Chiaki et al. (2013), however, assume a single size and a single component of dust ($MgSiO_3$, enstatite) which may be too simple as a realistic dust model in the early Universe. Clearly, further studies of the thermal evolution of the collapsing clouds based on more realistic dust models are necessary to clarify the formation condition of the first low-mass stars.

There are two leading studies that independently predict the size distribution and the total amount of dust ejected from Pop III supernovae with a wide range of progenitor masses: the models of N07 and S12. Both of the studies treat the formation of dust in the expanding ejecta and the destruction of dust by the reverse shocks, but present different compositions, size distributions, and masses of dust. Thus, the fragmentation condition can be different for the two dust models. In this paper, we explore the thermal evolution of low-metallicity star-forming clouds by employing these two sets of supernova dust models and by taking into account the growth of multiple grain species with size distributions.

In Section 2, we describe our one-zone model of the cloud evolution and the calculation of grain growth. In Section 3, we discuss the effect of grain growth on the thermal evolution of clouds. Then, we present the critical abundances of heavy elements for the formation of low-mass fragments. Concluding remarks and discussion are given in Section 4.

2 NUMERICAL METHOD

2.1 Collapse model and gas-phase chemistry

We follow the evolution of the cloud temperature T along with the increasing density calculated by a one-zone semi-analytic collapse model of Omukai (2000). In this paper, the cloud density is described as the hydrogen number density $n_{\rm H} = X_{\rm H}\rho/m_{\rm H}$, where $X_{\rm H}$ is the hydrogen mass fraction, ρ is the total (gas and dust) mass density, and $m_{\rm H}$ is the mass of a hydrogen atom. We include in this model non-equilibrium gas chemistry of eight species of primordial elements H^+, e^-, H, H^-, H_2, D^+, D, and HD, and 19 species made of heavy elements C^+, C, CH, CH_2, CO^+, CO, CO_2, O^+, O, OH^+, OH, H_2O^+, H_2O, H_3O^+, O_2^+, O_2, Si, SiO, and SiO_2. We solve the reduced chemical networks of Omukai, Hosokawa & Yoshida (2010) supplemented with the silicon chemistry. For species containing silicon, oxidation of Si and SiO is considered as the major reactions. Table 1 and Fig. 1 present the gas-phase chemical reactions of silicon and the rate coefficients used in this work. We also

Table 1. Silicon chemical reactions.

No.	Reaction	Rate coef.	Ref.
Si1	$Si + OH \rightarrow SiO + H$	3×10^{-11}	H80
Si2	$Si + O_2 \rightarrow SiO + O$	$1.3 \times 10^{-11} \exp(-111/T)$	LG90
Si3	$SiO + OH \rightarrow SiO_2 + H$	2×10^{-13}	H80

Note: The units of temperature T and rate coefficients are K and $cm^3\ s^{-1}$, respectively. Ref.: H80, Hartquist, Dalgarno & Oppenheimer (1980); LG90, Langer & Glassgold (1990).

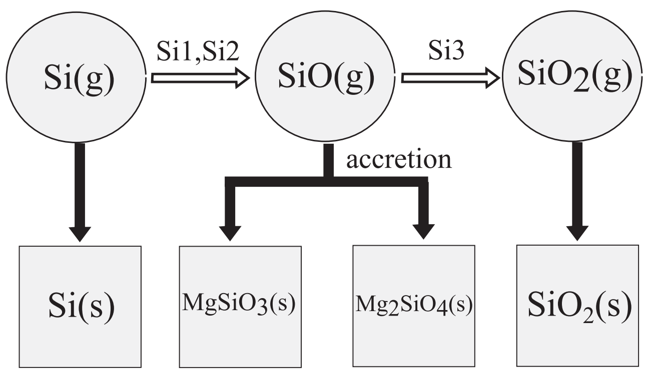

Figure 1. Chemical network of silicon (white arrows) which are included in our one-zone calculations. We also consider accretion of gas-phase species on to grains (indicated by black arrows). The reaction tabs above the arrows are identical with the reaction numbers in Table 1. Circles and squares depict gas-phase (g) and solid-phase (s) species, respectively.

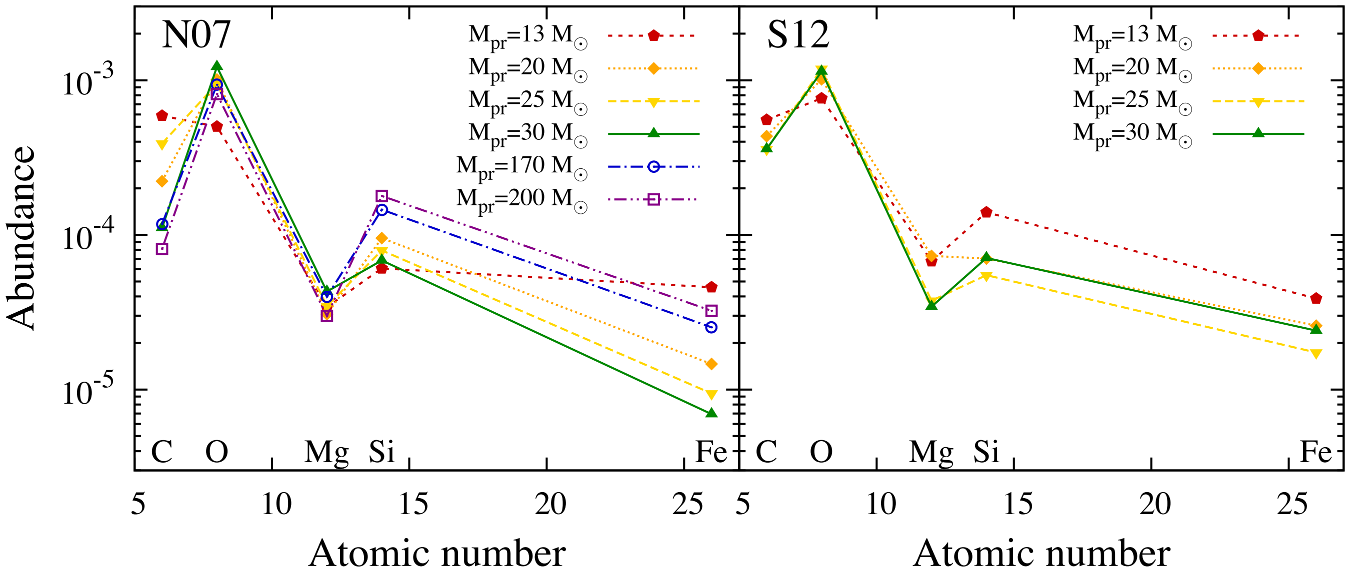

Figure 2. Number abundance A_j of heavy element j for the Pop III supernova models of N07 (left) and S12 (right). We plot the values derived by equation (1) with $Z = Z_{\odot}$. For each supernova model, red pentagons, orange diamonds, yellow opposite triangles, green triangles, blue circles, and purple squares show the abundances for supernovae with progenitor masses 13, 20, 25, 30, 170, and 200 $M_{\odot}$, respectively.

solve the cooling rates by emission lines of atoms/ions (C I, C II, and O I), and by molecules (H_2, HD, CO, OH, and H_2O). When the cloud becomes optically thick, the cooling rate from each line is reduced by the corresponding escape fraction. To this end, we determine the column density assuming the size of the cloud to be given by the Jeans length.

We set the initial hydrogen number density and temperature $n_{\rm H,0} = 0.1\,{\rm cm}^{-3}$ and $T_0 = 300\,{\rm K}$, respectively.[1] The initial number abundances of H^+ and H_2 relative to hydrogen nuclei are $y_0(H^+) = 10^{-4}$ and $y_0(H_2) = 10^{-6}$. The total number abundances of deuterium and helium are 3.0×10^{-5} and 0.083 (corresponding to the mass fraction $Y_{\rm He} = 0.25$), respectively. We assume that elements C, O, and Si are initially in the form of C^+ ions, neutral O atoms and Si atoms, respectively.

We consider the clouds to be enriched by Pop III supernovae. The supernova models give the mass yield M_j of heavy element j and the total metal yield $M_{\rm metal} = \sum M_j$. Pop III supernovae are generally characterized by metallicities in the range 1–30 $Z_{\odot}$ (Umeda & Nomoto 2002; Limongi & Chieffi 2012). Heavy elements are diluted within the expanding ejecta and eventually mixed with the ambient primordial gas. Thus, the formation site of the second-generation stars, polluted with the metal and dust, has typically a lower metallicity than the solar value. Setting the cloud metallicity Z as an effective dilution factor, we obtain the number abundance of heavy element j relative to hydrogen nuclei in the cloud as

$$A_j = \frac{Z}{\mu_j X_{\rm H}} \frac{M_j}{M_{\rm metal}}, \qquad (1)$$

where μ_j is the molecular weight of element j, and $X_{\rm H} = 1 - Y_{\rm He}$ is the hydrogen mass fraction.

Both N07 and S12 employ the core-collapse supernova (CCSN) models with progenitor masses $M_{\rm pr} = 13$, 20, 25, and 30 $M_{\odot}$ (hereafter called M13, M20, M25, and M30 models, respectively). N07 further explore the pair-instability supernova (PISN) models with $M_{\rm pr} = 170$ (M170) and 200 $M_{\odot}$ (M200). S12 adjust the mass cut, for each SN model, in order to fit the abundance pattern of the most primitive star SDSS J102915+172927 (Caffau et al. 2011). Such a procedure, as well as the properties of each progenitor mass and explosion details, has been extensively explained in Limongi & Chieffi (2012). Fig. 2 shows the abundances of the major heavy elements for various progenitor masses. For all the progenitor models, the abundances deviate from the solar values by ~0.5 dex. While S12 model can predict the abundances less sensitive to the progenitor mass, N07 model presents the various patterns. N07M13 models predict C > O, and heavier elements such as Si and Fe increase with the increasing progenitor mass.

2.2 Dust models

2.2.1 *Dust properties*

We consider 10 dust species: silicon (Si), iron (Fe), forsterite (Mg_2SiO_4), enstatite ($MgSiO_3$), magnetite (Fe_3O_4), amorphous carbon (C), silica (SiO_2), magnesia (MgO), troilite (FeS), and alumina (Al_2O_3). Note that, depending on the employed supernova models, some of the species are not efficiently formed in the supernova ejecta, or are fully destroyed by the reverse shocks.

We quantify the amount of dust grains by the condensation efficiency f_{ij}, which is defined as the number fraction of nuclei of element j locked in dust species i.[2] By using the condensation efficiency, the mass density of dust species i in the cloud is written as $\rho_i = f_{ij} A_j n_{\rm H} \mu_{ij} m_{\rm H}$, where μ_{ij} is the molecular weight of the grain species i per nucleus of element j (see Table 2).

In this study, we introduce the differential size distribution function $\varphi_i(r)$ of grain species i normalized as $\int \varphi_i(r) dr = 1$. Then, the number of dust particles per unit volume is

$$n_i = \frac{\rho_i}{(4\pi/3) s_i \int r^3 \varphi_i(r) {\rm d}r}, \qquad (2)$$

where s_i is the bulk density of an individual dust particle derived from the values of μ_{ij} and $a_{ij,0}$ in Table 2. We can calculate the number density of grains with radii between r and $r + dr$ as $n_i \varphi_i(r) dr$.

[1] Hereafter, the subscript '0' is referred to as the initial values.

[2] In this paper, the subscripts i and j denote grain species and heavy elements, respectively.

Table 2. Grain species considered in the calculations.

Grains	Key species	Chemical reaction	μ_{ij}	$a_{ij,0}$ (Å)
Si(s)	Si(g)	Si(g)→ Si(s)	28.0	1.684
Fe(s)	Fe(g)	Fe(g)→ Fe(s)	56.0	1.411
Mg_2SiO_4(s)	Mg(g)	2Mg(g) + SiO(g) + $3H_2O$(g) → Mg_2SiO_4(s) + $3H_2$(g)	70.0	2.055
	SiO(g)	2Mg(g) + SiO(g) + $3H_2O$(g) → Mg_2SiO_4(s) + $3H_2$(g)	140.0	2.589
$MgSiO_3$(s)	Mg(g), SiO(g)	Mg(g) + SiO(g) + $2H_2O$(g) → $MgSiO_3$(s) + $2H_2$(g)	100.0	2.319
Fe_3O_4(s)	Fe(g)	3Fe(g) + $4H_2O$(g) → Fe_3O_4(s) + $4H_2$(g)	77.3	1.805
C(s)	C(g)	C(g)→ C(s)	12.0	1.281
SiO_2(s)	SiO_2(g)	SiO_2(g)→ SiO_2(s)	60.0	2.080
MgO(s)	Mg(g)	Mg(g) + H_2O(g) → MgO(s) + H_2(g)	40.0	1.646
FeS(s)	Fe(g), S(g)	Fe(g) + S(g) → FeS(s)	88.0	1.932
Al_2O_3(s)	Al(g)	2Al(g) + $3H_2O$(g) → Al_2O_3(s) + $3H_2$(g)	51.0	1.718

Note: The subscripts '(s)' and '(g)' are attached to solid- and gas-phase species, respectively. The values are taken from Nozawa et al. (2003). μ_{ij} and $a_{ij,0}$ are the molecular weight and the hypothetical radius of a monomer molecule of grain species i per nuclei of the key element j.

2.2.2 H_2 formation on grains

In the presence of dust grains, H_2 molecules are efficiently formed on grain surfaces. Since H_2 molecules are major coolants in a low-metallicity gas, the thermal evolution of the collapsing gas is significantly affected (especially in the early stages of collapse) by the amount of dust. The formation rate of hydrogen molecules per grain of species i with radius r is

$$\mathcal{R}_{\mathrm{H_2},i}(r) = \frac{1}{2} n(\mathrm{H_I}) \langle v_\mathrm{H} \rangle \pi r^2 \epsilon_{\mathrm{H_2}} S_\mathrm{H}, \tag{3}$$

where $n(x)$ is the number density of gas-phase chemical species x, $\langle v_\mathrm{H} \rangle = (8kT/\pi m_\mathrm{H})^{1/2}$ is the average velocity of hydrogen atoms, $\epsilon_{\mathrm{H_2}}$ is the efficiency of H_2 recombination on grain surfaces, and S_H is the sticking efficiency of hydrogen atoms impacting grain surfaces (Cazaux & Tielens 2002). The values of $\epsilon_{\mathrm{H_2}}$ and S_H are functions of both gas and grain temperatures (see Schneider et al. 2006, for detailed formulation). We calculate $\mathcal{R}_{\mathrm{H_2},i}(r)$ for each dust species and each grain radius. Then, the formation rate of hydrogen molecules on grain surfaces per unit volume is described as

$$\left. \frac{\mathrm{d}n_{\mathrm{H_2}}}{\mathrm{d}t} \right|_{\text{on grains}} = \sum_i \int \mathcal{R}_{\mathrm{H_2},i}(r) n_i \varphi_i(r) \mathrm{d}r. \tag{4}$$

2.2.3 Dust temperature and cooling

The temperature $T_i(r)$ of grain species i with radius r can be derived from the balance between the heating by collisions with the gas particles (mostly hydrogen and helium atoms and electrons) and the cooling by thermal emission of dust. We ignore the heat exchange among dust particles because the grain–grain collision rate is much smaller than the gas–grain collision rate in the low metallicity environments considered in this paper. The heating rate of a dust grain with radius r owing to collisions with the gas particles is

$$\mathcal{G}_i(r) = \pi r^2 \langle n v_\mathrm{g} \rangle [2kT - 2kT_i(r)], \tag{5}$$

where $\langle n v_\mathrm{g} \rangle = [n(\mathrm{H_I}) + n(\mathrm{H_2})/\sqrt{2} + n(\mathrm{He_I})/2](8kT/\pi m_\mathrm{H})^{1/2}$ is the average velocity of gas particles. The cooling rate of a grain through thermal radiation is

$$\mathcal{L}_i(r) = 4\sigma_\mathrm{B} T_i^4(r) \left\langle Q_i^\nu(r) \right\rangle \pi r^2 \beta_\mathrm{cont}, \tag{6}$$

where σ_B is the Stephan–Boltzmann coefficient, $\langle Q_i^\nu(r) \rangle$ is the Planck-mean of the absorption coefficient, and β_cont is the continuum escape fraction (see the next section). From the energy balance equation of a dust grain, $\mathcal{G}_i(r) = \mathcal{L}_i(r)$, we can obtain dust temperature for each dust species and size. Then, the cooling rate of the gas owing to dust per unit volume is calculated by summing up equation (6) over all sizes and species:

$$\Lambda_\mathrm{d} = \sum_i \int \mathcal{L}_i(r) n_i \varphi_i(r) \mathrm{d}r. \tag{7}$$

2.2.4 Continuum opacity

The Planck-mean absorption coefficients of the grain species are taken from the references in table 1 of Nozawa et al. (2008). The continuum optical depth is

$$\tau_\mathrm{cont} = \left(\kappa_\mathrm{g} \rho_\mathrm{g} + \sum_i \int \left\langle Q_i^\nu(r) \right\rangle \pi r^2 n_i \varphi_i(r) \mathrm{d}r \right) l_\mathrm{sh}, \tag{8}$$

where κ_g is the Planck opacity of gas taken from Mayer & Duschl (2005), and $\rho_\mathrm{g} = \rho - \sum_i \rho_i$ is the mass density of gas-phase species. We calculate the shielding length l_sh as in Omukai (2000). Then, the escape fraction of continuum emission is calculated as $\beta_\mathrm{cont} = \min\{1, \tau_\mathrm{cont}^{-2}\}$ (Omukai 2000).

2.2.5 Grain growth

We consider that the grain growth by the accretion of the gas species proceeds via the reactions in Table 2. Here, we assume that the heavy element species with the smallest time-scale of collisions with grains control the kinetics of grain growth (hereafter, referred to as *key species*). In this model, silicon, silicates (forsterite and enstatite), and silica grains grow through the accretion of Si atoms, SiO molecules, and SiO_2 molecules, respectively, as indicated by filled arrows in Fig. 1. The flow of silicon from the gas phase to the solid phase is shown in Fig. 1, along with the gas phase reactions.

The growth rate of grain radius is given by

$$\left(\frac{\mathrm{d}r}{\mathrm{d}t} \right)_i = \alpha_i \left(\frac{4\pi}{3} a_{ij,0}^3 \right) \left(\frac{kT}{2\pi m_{i1}} \right)^{1/2} n_{i1}(t), \tag{9}$$

where α_i denotes the sticking probability of the gaseous species incident on to surfaces of grains i, and $a_{ij,0}$ denotes the hypothetical radius of a monomer molecule of grain species i in the dust phase, and m_{i1} and n_{i1}, respectively, denote the mass and the number density of the key species $i1$. We here assume the sticking probability $\alpha_i = 1$ (see Section 4 for the justification of the select of this value and for

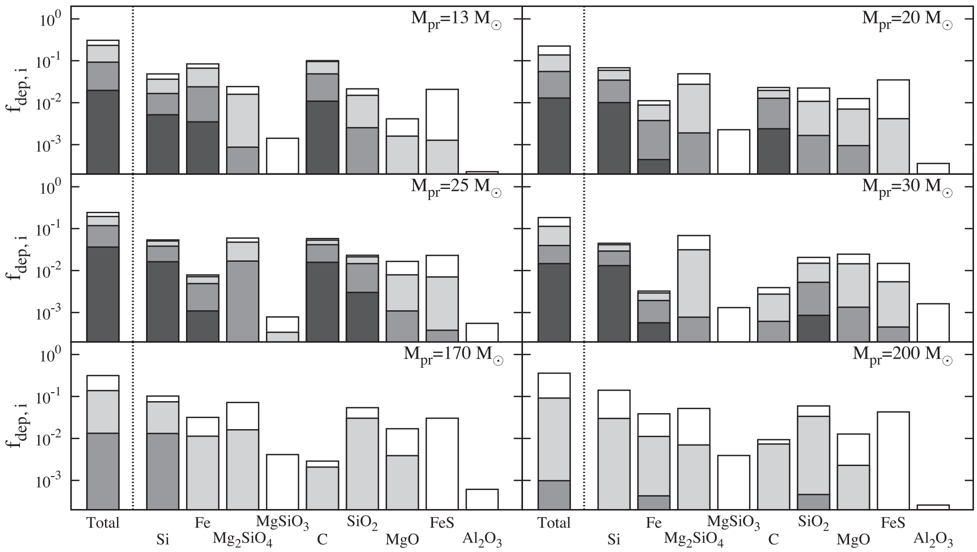

Figure 3. Mass fraction $f_{\mathrm{dep},i}$ of grain species i relative to the total metal mass for supernova model of N07. Each histogram represents the mass fraction for n0, n0.1, n1, and n10 model from top to bottom. The first histogram represents the depletion factor f_{dep} whereas the other histograms show the contribution of each dust species.

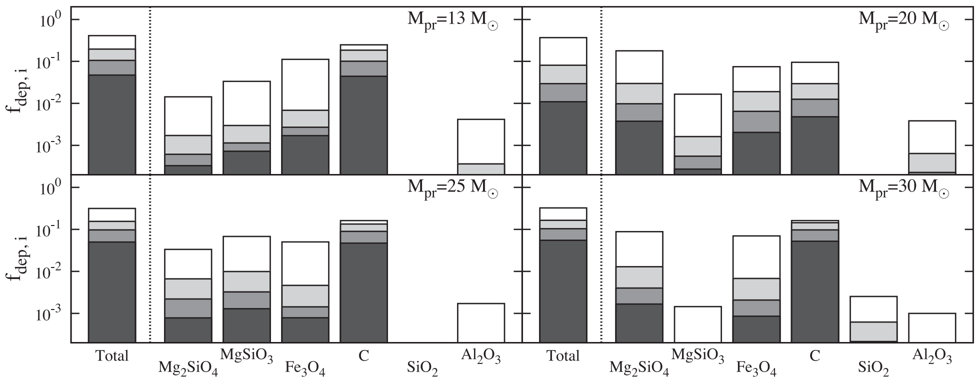

Figure 4. Same as Fig. 3 but for models by S12.

the effect of smaller α_i on the results). Note that the growth rate does not depend on the grain radius r. Therefore, the size distribution $\varphi_i(r, t)$ at a time t is equivalent to the initial one $\varphi_{i,0}(r)$ shifted to larger radii by $\Delta r = \int_0^t (\mathrm{d}r/\mathrm{d}t)_i \mathrm{d}t$. Then, the time evolution of the condensation efficiency is given as

$$f_{ij}(t) = f_{ij,0} \frac{\int r^3 \varphi_i(r,t) dr}{\int r^3 \varphi_{i,0}(r) \mathrm{d}r}. \tag{10}$$

The density $n(x_j)$ of the gas-phase species x_j containing the element j is determined by the condensation of the element j on to all the relevant grain species i as $n(x_j, t + \Delta t) = n(x_j, t) - \sum_i \{f_{ij}(t + \Delta t) - f_{ij}(t)\} A_j n_{\mathrm{H}}$ as well as the relevant gas-phase chemistry.

2.3 Supernova dust models

N07 and S12 calculate the formation of grains in the supernova ejecta for different progenitor masses, predicting the composition and size distribution of newly-formed grains, hereafter called n0 and norev models for N07 and S12, respectively. For each dust formation model, they also study dust destruction by reverse shocks which occurs after the grain formation. The strength of the reverse shock is parametrized with the density of the ambient gas around the supernovae. N07 investigate the reverse shock models when the number densities of the ambient gas is $n_{\mathrm{amb}} = 0.1$, 1, and $10\,\mathrm{cm}^{-3}$. We call these models n0.1, n1, and n10, respectively. S12 investigate for the mass densities of the ambient gas $\rho_{\mathrm{amb}} = 10^{-25}$ (rev1), 10^{-24} (rev2), and $10^{-23}\,\mathrm{g\,cm}^{-3}$ (rev3).

These models give the mass M_i of grain species i surviving against the destruction by the reverse shocks. Figs 3 and 4 show the ratio $f_{\mathrm{dep},i}$ of dust mass to the total metal mass for N07 and S12 models, respectively. Table 3 shows the values for carbon and silicate. One can see that the dust mass decreases with the increasing ambient gas density. We can also calculate the initial condensation efficiency of the collapsing cloud as

$$f_{ij,0} = \frac{M_i/\mu_{ij}}{M_j/\mu_j}. \tag{11}$$

The efficiency of gas cooling is determined by the dust composition and size distribution. N07 and S12 obtain different dust compositions. First, the mass fraction of carbon grains is generally larger for S12 model than N07 model. Carbon grains are formed by condensation of carbon atoms that are not oxidized to form CO molecules in the supernova ejecta. S12 consider the molecular destruction by the collision with high-energy electrons from ^{56}Co

Table 3. Initial values for supernova models and the critical conditions without grain growth.

Model	$M_{\rm pr}$	rev.	$f_{\rm dep,C,0}$	$S_{\rm C,0}$	$f_{\rm dep,Sil,0}$	$S_{\rm Sil,0}$	$f_{\rm dep,0}$	$\mathcal{D}_0$	$\mathcal{D}_{\rm cr,ng}$	$[Z_{\rm cr,ng}]$
N07M13n0	13	n0	**0.101**	**2.65**	0.024	3.83	0.305	6.106	3.060	− 5.3
N07M13n0.1		n0.1	**0.096**	**2.64**	0.016	2.77	0.233	4.659	2.335	− 5.3
N07M13n1		n1	**0.049**	**2.50**	<0.001	3.76	0.093	1.851	2.330	− 4.9
N07M13n10		n10	**0.011**	**3.88**	<0.001	7.77	0.020	0.392	1.966	− 4.3
N07M20n0	20	n0	0.023	4.51	**0.049**	**4.22**	0.220	4.402	2.777	− 5.2
N07M20n0.1		n0.1	**0.020**	**3.46**	**0.028**	**2.96**	0.137	2.750	3.462	− 4.9
N07M20n1		n1	**0.013**	**1.96**	0.002	3.61	0.055	1.110	5.563	− 4.3
N07M20n10		n10	**0.002**	**2.24**	<0.001	4.87	0.013	0.259	8.199	− 3.5
N07M2513n0	25	n0	**0.058**	**2.42**	**0.060**	**3.53**	0.240	4.797	3.810	− 5.1
N07M25n0.1		n0.1	**0.053**	**1.91**	**0.048**	**1.42**	0.195	3.907	3.907	− 5.0
N07M25n1		n1	**0.041**	**1.12**	0.017	1.35	0.118	2.351	4.692	− 4.7
N07M25n10		n10	**0.016**	**0.83**	<0.001	3.05	0.036	0.726	4.578	− 4.2
N07M30n0	30	n0	0.004	6.85	**0.068**	**3.99**	0.184	3.671	2.916	− 5.1
N07M30n0.1		n0.1	0.003	7.14	**0.031**	**4.04**	0.113	2.265	3.590	− 4.8
N07M30n1		n1	<0.001	10.27	<0.001	8.57	0.040	0.791	6.280	− 4.1
N07M30n10		n10	<0.001	7.52	<0.001	7.17	0.015	0.292	11.639	− 3.4
N07M170n0	170	n0	0.003	4.66	**0.072**	**6.62**	0.315	6.297	3.156	− 5.3
N07M170n0.1		n0.1	0.002	4.88	0.016	4.76	0.138	2.761	4.377	− 4.8
N07M170n1		n1	<0.001	10.03	<0.001	1.27	0.013	0.266	16.796	− 3.2
N07M170n10		n10	<0.001	12.31	0.000	–	<0.001	0.001	1.488	> − 2.0
N07M200n0	200	n0	0.009	5.39	**0.052**	**9.29**	0.359	7.189	3.603	− 5.3
N07M200n0.1		n0.1	0.007	5.20	0.007	4.94	0.091	1.824	2.892	− 4.8
N07M200n1		n1	**< 0.001**	**15.37**	<0.001	1.60	<0.001	0.020	4.935	− 2.6
N07M200n10		n10	<0.001	18.02	0.000	–	<0.001	<0.001	<0.001	> − 2.0
S12M13norev	13	norev	0.249	4.59	0.033	45.76	0.413	8.260	0.826	− 6.0
S12M13rev1		rev1	**0.185**	**3.35**	0.003	53.73	0.197	3.947	1.571	− 5.4
S12M13rev2		rev2	**0.101**	**3.22**	0.001	52.36	0.106	2.117	1.336	− 5.2
S12M13rev3		rev3	**0.044**	**3.28**	<0.001	47.14	0.047	0.943	1.494	− 4.8
S12M20norev	20	norev	**0.095**	**37.56**	**0.179**	**14.68**	0.369	7.384	0.738	− 6.0
S12M20rev1		rev1	**0.030**	**32.77**	**0.030**	**18.12**	0.081	1.618	0.811	− 5.3
S12M20rev2		rev2	**0.013**	**27.85**	0.010	18.22	0.030	0.591	0.937	− 4.8
S12M20rev3		rev3	**0.005**	**23.72**	0.004	17.00	0.011	0.219	1.098	− 4.3
S12M25norev	25	norev	**0.162**	**11.51**	**0.068**	**29.42**	0.315	6.293	0.997	− 5.8
S12M25rev1		rev1	**0.134**	**3.49**	**0.010**	**34.48**	0.155	3.106	2.467	− 5.1
S12M25rev2		rev2	**0.090**	**2.32**	**0.003**	**34.39**	0.097	1.934	2.435	− 4.9
S12M25rev3		rev3	**0.047**	**2.04**	0.001	33.17	0.050	1.000	2.512	− 4.6
S12M30norev	30	norev	0.161	1.44	**0.088**	**26.22**	0.324	6.485	1.629	− 5.6
S12M30rev1		rev1	**0.144**	**1.12**	**0.013**	**31.72**	0.164	3.285	2.609	− 5.1
S12M30rev2		rev2	**0.097**	**1.15**	**0.004**	**32.36**	0.104	2.071	2.607	− 4.9
S12M30rev3		rev3	**0.052**	**1.18**	**0.002**	**28.84**	0.055	1.094	2.182	− 4.7

Note: Progenitor mass $M_{\rm pr}$ is in the unit of $\mathrm{M}_{\odot}$. The third column 'rev.' refers to the reverse shock model (see text). $f_{{\rm dep},i,0}$ is the initial mass fraction of grain species i relative to the total metal mass and $S_{i,0}$ is the initial geometrical cross-section of grain i per unit dust mass ($\times 10^4\ {\rm cm^2\ g^{-1}}$). We write $f_{{\rm dep},i,0}$ and $S_{i,0}$ in bold if either carbon or silicate dust is the dominant coolant for each model. For silicate grains (i = Sil), we show the values for the dominant species: $MgSiO_3$ for S12M13 and S12M25 models, and Mg_2SiO_4 for the other models. $\mathcal{D}_0$ is the dust-to-gas mass ratio for our $Z = 10^{-5}\ \mathrm{Z}_{\odot}$ calculations ($\times 10^{-8}$). $\mathcal{D}_{\rm cr,ng}$ and $Z_{\rm cr,ng}$ are the critical dust-to-gas mass ratio and metallicity which we determine by one-zone calculations without grain growth ($[Z_{\rm cr,ng}] = \log{(Z_{\rm cr,ng}/\mathrm{Z}_{\odot})}$). Since we set metallicities varying every 0.1 dex, the value $[Z_{\rm cr,ng}] = -5.9$ indicates, for example, that fragmentation condition is met at $[Z_{\rm cr,ng}] \geq -5.9$, but not for $[Z_{\rm cr,ng}] \leq -6.0$.

(Todini & Ferrara 2001). N07 do not include the dissociation of the molecules. Although carbon grains are formed in the outer layers with C > O in the ejecta, most of the carbon nuclei are in the inner layers, where oxygen nuclei are also abundant. Thus, the formation of carbon grains is mitigated in N07 model.

Secondly, magnetite grains are produced only in S12 models. This results from the different ejecta models. Our N07 model is taken from their unmixed ejecta model, where the ejecta is considered to remain stratified, i.e. keeping the original onion-like structure of composition of heavy elements during the explosions. While the oxygen-rich layer is originally in the outer region, Fe is in the innermost layer. In this case, Fe_3O_4 grains are not formed because of the assumed inefficient mixing. On the other hand, S12 assume the fully mixed ejecta, where the composition of heavy elements is uniform, and magnetite grains can be formed.

N07 and S12 models also produce different size distribution functions. In Fig. 5, we compare the initial size distributions of Mg_2SiO_4 grains for the two extreme cases: without dust destruction (n0 and norev) and with the largest efficiency of the dust destruction among their reverse shock models (n10 and rev3). The size distribution of newly formed grains is mainly regulated by the number density of condensable gas species, i.e. elemental composition at the

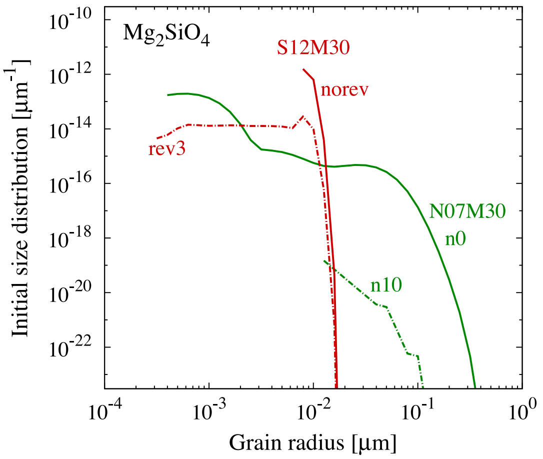

Figure 5. Initial size distribution of Mg_2SiO_4 grains for the N07 (green) and S12 (red) models without the effect of dust destruction (solid) and with the largest efficiency of dust destruction among the three reverse shock models (dot–dashed).

formation site of the grains. For the dust model by S12, where the uniform elemental composition in the ejecta is assumed, the size distribution of newly formed grains is confined to a narrow range of grain radius (see the red solid curve in Fig. 5). On the other hand, in the unmixed ejecta applied by N07, dust grains form with different characteristic radii in the layers with the different elemental compositions. Thus, the resulting size distribution, which is made of the contributions of grains formed in each formation region, spreads in a wider range of radius than S12 model (green solid curve).

The successive process of dust destruction also affects the size distribution of surviving grains. S12 assume that the grains are trapped in the high-temperature region defined by the reverse and forward shocks, where the grains undergo sputtering by the impact of high-energy ions. The grain size continues to decrease until the ejecta cools down sufficiently, and the size distribution of surviving dust has a flat tail at the smaller radii (see the red dot–dashed curve in Fig. 5). N07 consider the relative motion between the expanding gas and dust grains. The erupted dust grains are decelerated by the drag force from the gas. Smaller grains are more tightly coupled with the gas so that they remain in the shocked hot ejecta, continuing to be destroyed. Some of the grain species are totally destroyed and returned to the gas phase. Since larger grains are more likely to escape from the ejecta because of their larger inertia, they survive without being significantly destroyed. As a result, the size distribution is truncated at a given radius (green dot–dashed curve).

These different dust properties can affect the dust amount above which dust cooling activates the gas fragmentation: for S12 model, which predicts the smaller grain radii than N07, the efficiency of gas cooling by grains is expected to be larger because the total grain cross-section is larger with the fixed dust mass. In this paper, we define the critical condition for N07 and S12 supernova dust models separately. We consider the dust models where grains are not destroyed by reverse shocks (n0 and norev), and also three dust models where the reverse shock destruction is calculated for different ambient gas densities for each progenitor mass. In order to see the effect of grain growth, we study both cases with and without grain growth for each supernova dust model. We determine the critical dust amount by varying the gas metallicity in the range of $Z = 10^{-7}$–10^{-2} $Z_{\odot}$, where $Z_{\odot} = 0.02$.

3 RESULTS

3.1 Thermal evolution of gas clouds

We highlight and discuss the results of some specific cases in this section. Fig. 6 shows the thermal evolution of the cloud centre for our N07M30n1 model with metallicities $Z = 10^{-6}$, 10^{-5}, and 10^{-4} $Z_{\odot}$. Around $n_{\rm H} \sim 10^4$ cm^{-3}, H_2 cooling becomes efficient for a higher metallicity because H_2 molecules are formed on grain surfaces more efficiently. If the gas temperature drops below ~100 K, HD cooling becomes dominant (Omukai et al. 2005; Hirano et al. 2014), which can be seen at $n_{\rm H} \sim 10^4$–10^6 cm^{-3} with metallicities $Z > 10^{-5}$ $Z_{\odot}$. Then, OH ($Z \geq 10^{-5}$ $Z_{\odot}$) becomes a major coolant at $n_{\rm H} \sim 10^5$–10^8 cm^{-3}. For $Z = 10^{-5}$ and 10^{-4} $Z_{\odot}$, the gas temperature increases by the heating owing to the exothermic reaction of the formation of H_2 molecules via rapid three-body reactions at $n_{\rm H} = 10^9$–10^{12} cm^{-3}. If the amount of dust is sufficiently large, dust cooling becomes effective at $n_{\rm H} = 10^{11}$–10^{12} cm^{-3}.

We examine the condition for the formation of low-mass fragments by radiative cooling on the basis of the analysis by Schneider & Omukai (2010). First, the gas becomes gravitationally unstable and deformed due to rapid cooling when the specific heat ratio, γ, drops below unity. When the gas cooling is inefficient ($\gamma \gtrsim 1$) and the gas is likely to collapse in approximately a spherical manner, yielding fragments whose mass is about the Jeans mass corresponding to the gas density and temperature at the fragmentation (e.g. Larson 1985; Inutsuka & Miyama 1997). Then, the fragmentation condition for a gas cloud is defined as the following set of three criteria: (1) the gas cloud undergoes rapid radiative cooling ($\gamma < 0.8$), but then (2) gas cooling becomes soon inefficient ($\gamma > 0.97$). Since we are interested in the cases where low-mass fragments are formed, we add another criterion to our fragmentation condition: (3) the cloud Jeans mass is less than 0.8 $M_{\odot}$ when both (1) and (2) are satisfied.

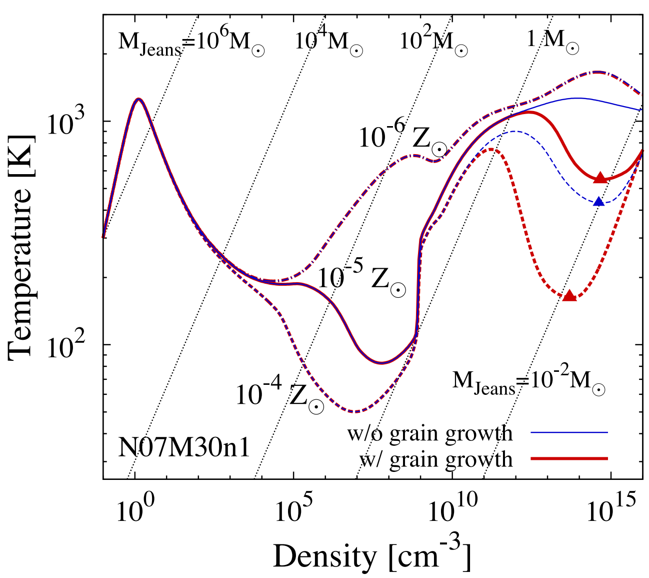

Figure 6. Temperature evolution as a function of the hydrogen number density of the cloud centres for our N07M30n1 model with metallicities $Z = 10^{-6}$ $Z_{\odot}$ (dot–dashed), 10^{-5} $Z_{\odot}$ (solid), and 10^{-4} $Z_{\odot}$ (dashed), respectively. Red thick and blue thin curves depict the cases with and without grain growth, respectively. Triangles are plotted at the states where the fragmentation condition (see text) is met.

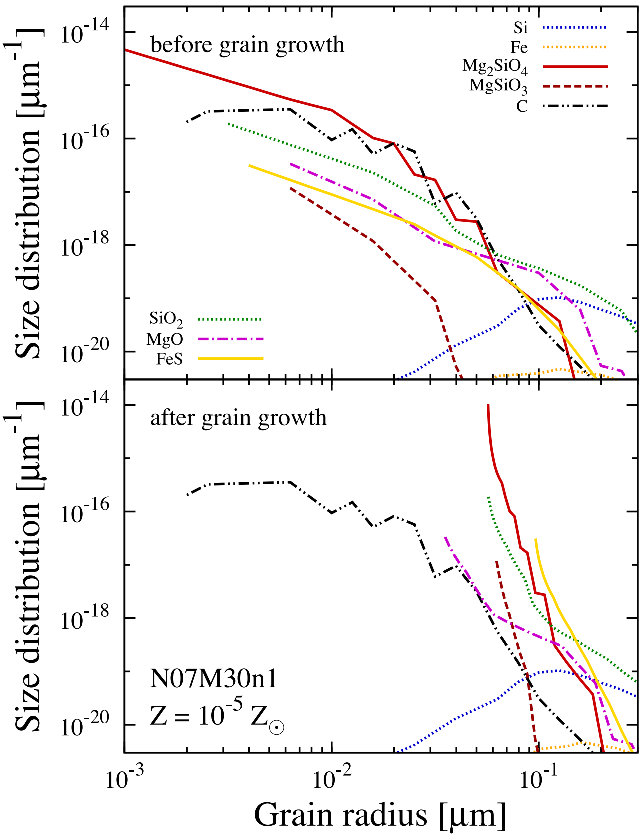

Figure 7. Size distribution function $n_i\varphi_i/n_{\rm H}$ of dust species i before ($n_{\rm H} = 0.1\,{\rm cm}^{-3}$) and after ($n_{\rm H} = 10^{16}\,{\rm cm}^{-3}$) grain growth for our N07M30n1 model with $Z = 10^{-5}\,{\rm Z}_{\odot}$. Size of all species but for C and Si grains increases by accretion of heavy elements. C and Si grains do not grow because the key species, C and Si atoms, are depleted on to CO and SiO molecules, respectively.

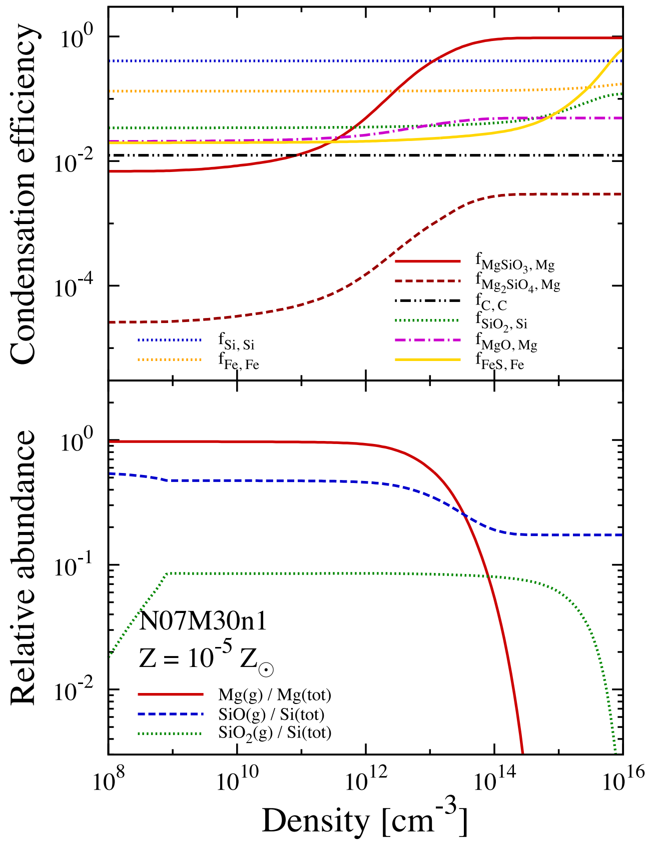

Figure 8. Top: number fraction of nuclei which are concentrated into grains i relative to total nuclei of element j in both the gas- and solid-phases (condensation efficiency f_{ij}). Bottom: number fraction of nuclei which are in the form of SiO molecules (blue dashed), and SiO_2 molecules (green dotted) relative to total Si nuclei. Red solid curves depict the number fraction of Mg in the gas phase to total Mg nuclei. This figure shows the evolution for the same case as Fig. 7.

In some models, we find O I cooling is efficient enough to trigger fragmentation, i.e. the criteria (1) and (2) given above are met, at $n_{\rm H} \sim 10^2$–$10^3\,{\rm cm}^{-3}$ for metallicities $Z \geq 10^{-4}\,{\rm Z}_{\odot}$. However, since the mass of the clump is $\sim$100 ${\rm M}_{\odot}$ in this regime, the criterion (3) is not satisfied (see Section 4 for the further discussion of this). It is clearly shown in Fig. 6 that dust cooling is effective at higher densities, $n_{\rm H} = 10^{12}$–$10^{15}\,{\rm cm}^{-3}$, where the Jeans mass is $\sim$0.01 ${\rm M}_{\odot}$. In this regime, all of the three criteria are met, suggesting that dust cooling can drive the fragmentation of the gas into small mass clumps.

Let us discuss the effect of grain growth in detail. Fig. 6 shows that, for $Z = 10^{-5}\,{\rm Z}_{\odot}$ (solid curves), the fragmentation condition is met with grain growth (red) while dust cooling is inefficient without grain growth (blue). For $Z = 10^{-4}\,{\rm Z}_{\odot}$ (dashed), the fragmentation condition is met even for the case without grain growth. Overall, the metallicity, or the initial amount of dust required for the gas fragmentation, is reduced by the effect of grain growth.

Fig. 7 shows the size distribution of grains for N07M30n1 model with $Z = 10^{-5}\,{\rm Z}_{\odot}$ before ($n_{\rm H} = 0.1\,{\rm cm}^{-3}$) and after ($10^{16}\,{\rm cm}^{-3}$) grain growth. We see that the radii of grains increase especially for Mg_2SiO_4 (red solid curve). If linearly plotting the figure, the distribution functions just shift from left to right because the increment of grain radii is independent from their initial radii as we have mentioned above. Fig. 8 shows the condensation efficiencies of grain species i (top) and the number fractions of Mg atoms, and SiO and SiO_2 molecules relative to total Mg and Si nuclei, respectively (bottom). The condensation efficiencies of all species but carbon (black dot-dot–dashed) and silicon (blue dotted) increase by accreting the gas-phase species. Almost all Si atoms are oxidized into SiO molecules at $n_{\rm H} < 10^8\,{\rm cm}^{-3}$, where silicate grains (Mg_2SiO_4 and $MgSiO_3$) grow most rapidly by accretion of Mg atoms and SiO molecules at $n_{\rm H} \sim 10^{11}$–$10^{13}\,{\rm cm}^{-3}$. Further, MgO grains grow almost at the same time as silicate until gas-phase magnesium is exhausted. Some fractions of SiO molecules survive without being incorporated into dust grains, because $A_{\rm Mg} < 2A_{\rm Si}$. SiO_2 molecules fully condense into SiO_2 grains at $n_{\rm H} \gtrsim 10^{15}\,{\rm cm}^{-3}$. Even if SiO_2 molecules are totally depleted, SiO molecules are not further oxidized because the major oxidizer, OH, is already depleted into H_2O. At $n_{\rm H} \sim 10^{15}\,{\rm cm}^{-3}$, FeS grains begin to grow. The time when grains grow depends mostly on the abundances of gas-phase elements as well as the monomer radius $a_{ij,0}$. Carbon grains do not grow because C atoms have been already depleted into CO molecules at $n_{\rm H} = 10^6\,{\rm cm}^{-3}$. As a result of grain growth, at $n_{\rm H} = 10^{12}\,{\rm cm}^{-3}$, the total depletion factor (total mass fraction of dust relative to metal) increases from 0.040 to 0.045 and 0.14 for $Z = 10^{-5}$, and $10^{-4}\,{\rm Z}_{\odot}$, respectively.

Fig. 9 shows the contribution of each grain species to gas cooling as a function of gas density for N07M30n1 model. Without grain growth, Si and SiO_2 grains make a major contribution to gas cooling. On the other hand, the cooling rate of Mg_2SiO_4 grains is enhanced by accretion of heavy elements, and eventually becomes larger than

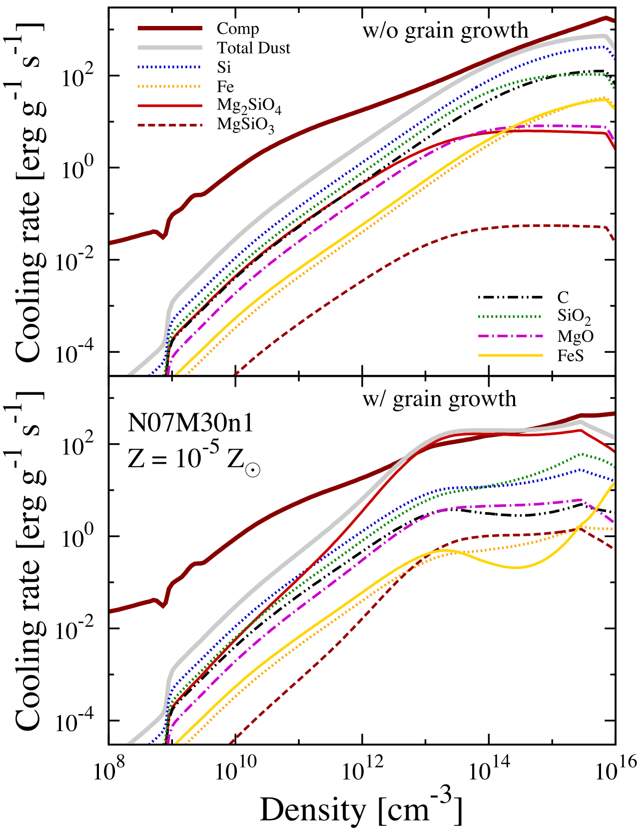

Figure 9. Gas cooling rate per unit gas mass owing to each dust species as a function of gas density with metallicity $Z = 10^{-5}\,\mathrm{Z}_{\odot}$ for N07M30n1 models with (top) and without (bottom) grain growth. We also plot the total dust cooling rate (thick grey) summed over all grain species and the gas compressional heating rate (thick dark red).

the compressional heating rate. This means that the small initial dust amount suffices for cloud fragmentation by the effect of grain growth.

3.2 Conditions for cloud fragmentation

3.2.1 Critical dust-to-gas mass ratio and metallicity

In this section, we discuss the results for all our dust models, and determine the conditions for the cloud fragmentation. First of all, we find that dust cooling triggers the gas fragmentation for the models where the fragmentation condition is satisfied. This indicates that the dust-to-gas mass ratio $\mathcal{D}$ is the key quantity to determine the fragmentation properties of the gas as suggested by S12. We first show the initial value $\mathcal{D}_0$ with $Z = 10^{-5}\,\mathrm{Z}_{\odot}$ in Table 3. The dust-to-gas mass ratio for arbitrary metallicity Z can be obtained simply by $(Z/10^{-5}\,\mathrm{Z}_{\odot})\mathcal{D}_0$. Then, varying the metallicity by 0.1 dex, we define the critical dust-to-gas mass ratios $\mathcal{D}_{\rm cr,ng}$ and $\mathcal{D}_{\rm cr,gg}$ above which dust cooling triggers the fragmentation into low-mass gas clumps, based on our one-zone calculations without and with grain growth as Tables 3 and 4 show, respectively. For almost all the models, the critical dust-to-gas mass ratio is reduced by the effect of grain growth. For example, for N07M30n1 model, $\mathcal{D}_{\rm cr,ng} = 6.3 \times 10^{-8}$ without grain growth, while it decreases to $\mathcal{D}_{\rm cr,gg} = 0.63 \times 10^{-8}$ with grain growth. The initial dust-to-gas mass ratio $\mathcal{D}_0$ for this case is 0.79×10^{-8} with $Z = 10^{-5}\,\mathrm{Z}_{\odot}$, which is lower than $\mathcal{D}_{\rm cr,ng}$ but higher than $\mathcal{D}_{\rm cr,gg}$. For all our supernova models, the critical dust-to-gas mass ratio is reduced from $\mathcal{D}_{\rm cr,ng} = [0.81 : 11.6] \times 10^{-8}$ to $\mathcal{D}_{\rm cr,gg} = [0.07 : 3.82] \times 10^{-8}$, depending on the dust model as we see in the next section. Note that we do not count n1 and n10 models for PISNe because the PISN models predict the much larger amounts of heavy elements such as Si and Fe than those inferred from the Galactic metal-poor stars so far observed, and because the ambient gas density of these progenitors is expected to be small $n_{\rm amb} \lesssim 0.1$–$1\,\mathrm{cm}^{-3}$ by the copious emission of ultraviolet photons in their main sequence (Kitayama et al. 2004; Whalen, Abel & Norman 2004).

If the dust amount is constant during the collapse of the gas clouds, the condition for gas fragmentation can be described simply by the initial dust-to-gas mass ratio (S12). We have shown that grain growth can alter this simple picture. If grains can completely accrete the gas-phase refractory elements, the condition becomes insensitive to the initial dust properties but sensitive to the gas metallicity because the depletion efficiency of metals on to dust grains converges to a certain value determined by the amounts of the refractory elements in this extreme case. To see how the fragmentation property depends on the metal and dust contents, let us study the dependence of the critical metallicity on the dust model. Although there are various quantities that characterize the dust for each supernova model, we here focus on the initial depletion factor. The metallicity $Z_{\rm cr}$ above which gas fragmentation is triggered is given by the relation $Z_{\rm cr} = \mathcal{D}_{\rm cr} f_{\rm dep,0}^{-1}$. The last column in Tables 3 and 4 shows the values $Z_{\rm cr,ng}$ and $Z_{\rm cr,gg}$ without and with grain growth, respectively, and Table 3 shows $f_{\rm dep,0}$. Without grain growth, the critical metallicity is roughly inversely proportional to the initial depletion factor as $Z_{\rm cr,ng} = \overline{\mathcal{D}_{\rm cr,ng}} f_{\rm dep,0}^{-1}$ with the average critical dust-to-gas mass ratio $\overline{\mathcal{D}_{\rm cr,ng}} = [2.0 : 2.5] \times 10^{-8}$. With grain growth, the least-squares fitting to the results for both N07 and S12 models leads to the following relationship:

$$\left(\frac{Z_{\rm cr,gg}}{10^{-5.5}\,\mathrm{Z}_{\odot}}\right) = \left(\frac{f_{\rm dep,0}}{0.18}\right)^{-0.44\pm0.21}. \qquad (12)$$

The critical metallicity is still dependent on the initial depletion factor, because the gas-phase heavy elements partly condense into dust grains as we discuss below. Note that the uncertainty of the spectrum index stems from the dependence of the critical metallicity on the composition, size distribution, and initial condensation efficiency of the dust models adopted in this paper as discussed in the next subsection.

Our study has shown that the grain growth is important to alter the fragmentation property for our supernova models. For the case with the least depletion factor (0.011) among our supernova dust models, $Z_{\rm cr}$ is reduced by about a factor of 20. We also find that the dust properties in the early star-forming regions are much different from those of the local Universe, where all refractory elements are depleted on to grains (Pollack et al. 1994).

3.2.2 Dependence of the critical metallicity on the initial dust models

We note that there are appreciable scatters in the critical metallicity from the average value of equation (12), depending on the initial dust properties. Fig. 10 shows $Z_{\rm cr}$ as a function of the initial depletion factor for N07 and S12 models separately.

We begin with the cases without grain growth. Open symbols in Fig. 10 present $Z_{\rm cr,ng}$, and the average values are drawn by the dotted lines. The critical metallicity roughly follows the relationship

Table 4. Critical conditions with grain growth.

Model	$M_{\rm pr}$	rev.	$r_{\rm Sil}^{\rm grow}$	$\log(n_{\rm H,Sil}^{\rm grow})$	$f_{\rm dep,Sil,*}$	$S_{\rm Sil,*}$	$f_{\rm dep,*}$	$\mathcal{D}_{\rm cr,gg}$	$[Z_{\rm cr,gg}]$
N07M13n0	13	n0	0.0060	no	0.024	3.83	0.351	0.769	− 5.9
N07M13n0.1		n0.1	0.0444	no	0.017	2.78	0.270	1.473	− 5.5
N07M13n1		n1	0.0331	15.2	0.001	3.95	0.128	0.928	− 5.3
N07M13n10		n10	0.0147	15.9	<0.001	8.45	0.043	0.312	− 5.1
N07M20n0	20	n0	0.0074	∗	**0.051**	**5.22**	0.224	2.777	− 5.2
N07M20n0.1		n0.1	0.0342	12.8	**0.034**	**3.12**	0.146	2.184	− 5.1
N07M20n1		n1	0.0313	14.0	**0.003**	**4.00**	0.057	1.397	− 4.9
N07M20n10		n10	0.0228	15.6	**< 0.001**	**5.25**	0.013	0.820	− 4.5
N07M2513n0	25	n0	0.0044	∗	**0.060**	**4.24**	0.241	3.810	− 5.1
N07M25n0.1		n0.1	0.0615	∗	**0.051**	**1.44**	0.200	3.103	− 5.1
N07M25n1		n1	0.0754	13.8	**0.020**	**1.39**	0.121	2.351	− 5.0
N07M25n10		n10	0.0511	15.0	**< 0.001**	**2.93**	0.036	1.448	− 4.7
N07M30n0	30	n0	0.0221	∗	**0.069**	**3.99**	0.184	2.916	− 5.1
N07M30n0.1		n0.1	0.0339	12.7	**0.044**	**4.01**	0.128	2.265	− 5.0
N07M30n1		n1	0.0120	13.2	**0.006**	**8.80**	0.045	0.628	− 5.1
N07M30n10		n10	0.0246	15.9	<0.001	5.43	0.015	0.734	− 4.6
N07M170n0	170	n0	0.0078	∗	**0.072**	**6.62**	0.317	3.156	− 5.3
N07M170n0.1		n0.1	0.0439	13.1	**0.029**	**4.07**	0.154	2.194	− 5.1
N07M170n1		n1	0.1813	no	**< 0.001**	**1.17**	0.013	2.662	− 4.0
N07M170n10		n10	–	–	0.000	–	<0.001	1.488	> − 2.0
N07M200n0	200	n0	0.0045	∗	**0.053**	**9.68**	0.364	3.603	− 5.3
N07M200n0.1		n0.1	0.0452	13.8	0.012	4.19	0.098	1.824	− 5.0
N07M200n1		n1	0.1440	no	<0.001	1.48	0.001	0.031	− 4.8
N07M200n10		n10	–	–	0.000	–	<0.001	<0.001	− 3.2
S12M13norev	13	norev	0.0051	10.4	**0.200**	**25.28**	0.602	0.826	− 6.0
S12M13rev1		rev1	0.0039	11.2	**0.203**	**14.62**	0.476	0.497	− 5.9
S12M13rev2		rev2	0.0040	11.6	**0.178**	**10.90**	0.333	0.336	− 5.8
S12M13rev3		rev3	0.0047	12.4	**0.069**	**10.79**	0.164	0.188	− 5.7
S12M20norev	20	norev	0.0159	∗	**0.179**	**14.68**	0.370	0.466	− 6.2
S12M20rev1		rev1	0.0115	11.1	**0.141**	**11.56**	0.242	0.204	− 5.9
S12M20rev2		rev2	0.0109	11.8	**0.107**	**9.24**	0.172	0.118	− 5.7
S12M20rev3		rev3	0.0118	12.4	**0.064**	**7.43**	0.105	0.069	− 5.5
S12M25norev	25	norev	0.0080	9.1	**0.086**	**27.19**	0.337	0.997	− 5.8
S12M25rev1		rev1	0.0061	11.5	**0.093**	**17.77**	0.259	0.982	− 5.5
S12M25rev2		rev2	0.0060	12.0	**0.074**	**13.58**	0.181	0.770	− 5.4
S12M25rev3		rev3	0.0061	12.3	**0.049**	**11.21**	0.105	0.501	− 5.3
S12M30norev	30	norev	0.0088	∗	**0.088**	**26.22**	0.325	1.629	− 5.6
S12M30rev1		rev1	0.0065	11.3	**0.068**	**19.56**	0.240	1.039	− 5.5
S12M30rev2		rev2	0.0062	12.0	**0.045**	**16.09**	0.157	0.825	− 5.4
S12M30rev3		rev3	0.0071	12.5	**0.024**	**13.24**	0.084	0.548	− 5.3

Note: $r_i^{\rm grow}$ is the characteristic size of grain species i for grain growth (μm; see text). $n_{{\rm H},i}^{\rm grow}$ is the density where the condensation efficiency of grain species i becomes above 0.5 by grain growth for $Z = 10^{-5}\,{\rm Z}_{\odot}$ runs (cm^{-3}). $n_{{\rm H},i}^{\rm grow}$ is not defined when the condensation efficiency is initially above 0.5 ('∗') or when the condensation efficiency does not reach 0.5 until $n_{\rm H} = 10^{16}\,{\rm cm}^{-3}$ ('no'). The subscript '∗' denotes the value for $Z = 10^{-5}\,{\rm Z}_{\odot}$ at density $n_{\rm H} = 10^{12}\,{\rm cm}^{-3}$. The critical dust-to-gas mass ratio $\mathcal{D}_{\rm cr,gg}$ and metallicity $Z_{\rm cr,gg}$ are determined by our one-zone calculations with grain growth.

$Z_{\rm cr,ng} = \mathcal{D}_{\rm cr,ng} f_{\rm dep,0}^{-1}$ with the specific value of $\mathcal{D}_{\rm cr,ng}$ for each progenitor mass. In more quantitative manner, we revisit the criterion of

$$S\mathcal{D} > 1.4 \times 10^{-3}\ {\rm cm}^2\ {\rm g}^{-1} \times \left(\frac{T}{10^3\ {\rm K}}\right)^{-1/2} \left(\frac{n_{\rm H}}{10^{12}\ {\rm cm}^{-3}}\right)^{-1/2},$$

where S is the total geometrical cross-section of grains per unit dust mass (S12). We rewrite the left-hand side as $S\mathcal{D} = Z \sum_i f_{{\rm dep},i} S_i$ to see the contributions of the dust composition and size distribution of different species. Here, $f_{{\rm dep},i} = \rho_i/\rho_{\rm metal} = f_{ij} A_j n_{\rm H} \mu_{ij} m_{\rm H}/\rho_{\rm metal}$ is proportional to the mass fraction of the grain species i. S_i is the cross-section of species i per unit dust mass as

$$S_i = \frac{\pi \left\langle r^2 \right\rangle_i}{(4\pi/3) s_i \left\langle r^3 \right\rangle_i} = \frac{3}{4 s_i r_i^{\rm cool}}, \tag{13}$$

where $r_i^{\rm cool} = \langle r^3 \rangle_i / \langle r^2 \rangle_i$ is an average dust radius characterizing dust cooling rate. This represents the contribution of the dust size distribution to gas cooling.

Table 3 shows $f_{{\rm dep},i}$ and S_i for the major species: carbon and silicate. For S12 model, the mass fraction of carbon grains is larger than N07 model as shown in the fourth column of Table 3. Although the mass fraction of silicate grains is similar between the two models,

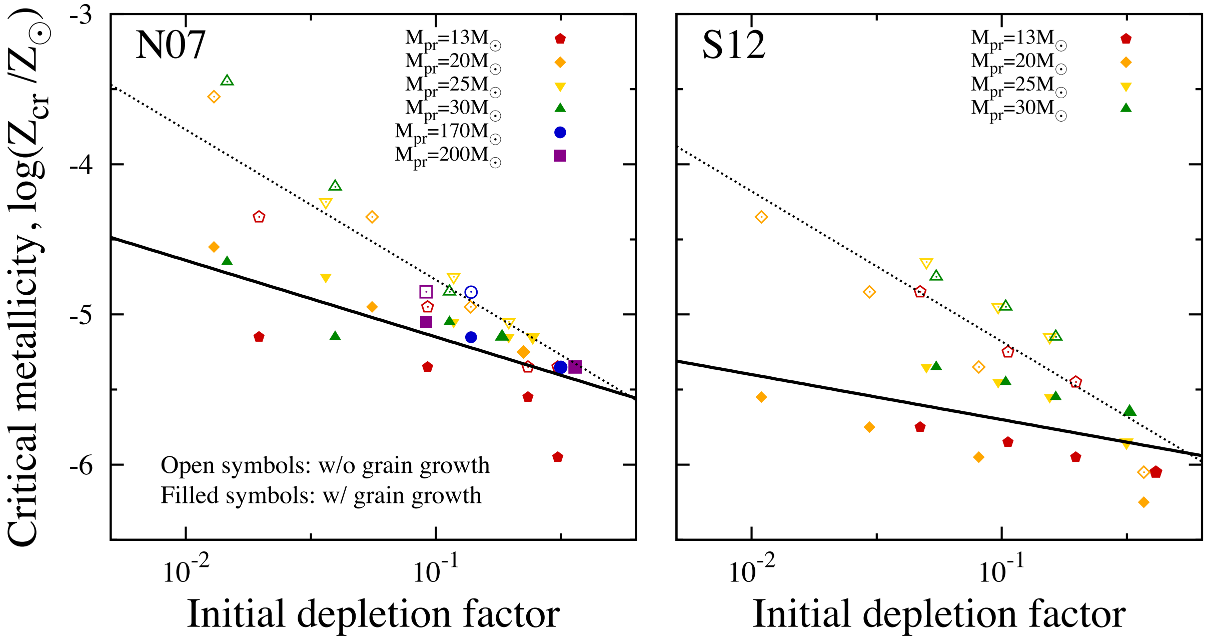

Figure 10. Critical metallicity $Z_{\rm cr}$ for N07 (left panel) and S12 (right) supernova dust models as a function of the initial dust-to-metal mass ratio (depletion factor), $f_{\rm dep,0}$. Four points with the same symbol (progenitor mass) correspond to our four reverse shock models: n0, n0.1, n1, and n10 from right to left. Open and filled symbols depict the results obtained by our one-zone calculations with and without grain growth, respectively. Dotted and solid lines are fitted to these results for each supernova model. The former are $Z_{\rm cr,ng} = 3.4 \times 10^{-8} f_{\rm dep,0}^{-1}$ and $Z_{\rm cr,ng} = 1.3 \times 10^{-8} f_{\rm dep,0}^{-1}$, and the latter $(Z_{\rm cr,gg}/10^{-5.5}\,{\rm Z_{\odot}}) = (f_{\rm dep,0}/0.50)^{-0.51}$ and $(Z_{\rm cr,gg}/10^{-5.5}\,{\rm Z_{\odot}}) = (f_{\rm dep,0}/0.022)^{-0.30}$ for N07 and S12 models, respectively.

the contribution of this species to gas cooling is different because the value $S_{\rm Sil,0}$ for S12 model is larger than N07 model as a result of the smaller characteristic size of silicate grains for the former case as we have seen in Fig. 5. The contribution of magnetite grains, whose cooling efficiency is also large, can reduce the critical metallicity for S12 model. Therefore, the total dust cooling efficiency is larger for S12 model and hence the lower initial dust amount suffices to activate the gas fragmentation.

The critical dust-to-gas mass ratio $\mathcal{D}_{\rm cr,ng}$ varies also with progenitor masses. For N07 model, this value is smallest for M13 models, followed by M25. This variation stems from the composition of the dominant species: carbon and silicate. For n0 cases, $\mathcal{D}_{\rm cr,ng}$ is rather insensitive to the progenitor mass because the sum of the contributions of carbon and silicate is similar to each other. On the other hand, for n10 cases, the cooling efficiency is largely determined by the mass fraction of carbon grains because silicate, which is more efficiently destroyed by the reverse shock than carbon, can no longer contribute to gas cooling (see Fig. 3). The fraction of carbon grains is largest for M13, and thus $\mathcal{D}_{\rm cr,ng}$ is smallest, followed by M25. For S12 model, the critical dust amount is sensitive to the dust size distribution of only carbon grains because this species is the dominant coolant. $\mathcal{D}_{\rm cr,ng}$ decreases roughly with the increasing $S_{\rm C,0}$.

With grain growth, the critical metallicity is reduced, as seen by the filled symbols in Fig. 10. The solid lines represent the results of the least-squares fitting as $Z_{\rm cr,gg} \propto f_{\rm dep,0}^{-0.51}$ and $f_{\rm dep,0}^{-0.30}$ for N07 and S12, respectively, showing that the effect of grain growth is larger for the latter case. We compare the density $n_{{\rm H},i}^{\rm grow}$ at which the condensation efficiency of grain i exceeds 0.5. Table 4 presents $n_{\rm H,Sil}^{\rm grow}$ for silicate grains, which grow most rapidly for most of our supernova models. For S12 model, $n_{\rm H,Sil}^{\rm grow}$ is below a density $n_{\rm H} \sim 10^{12}\,{\rm cm^{-3}}$ where dust cooling becomes efficient. On the other hand, for N07 model, grains can grow only after this threshold density. Thus, the cooling efficiency for N07 model is less modified by grain growth than S12 model especially for the cases with the dust destruction in the supernovae.

The growth rate of grains is determined by their composition and size. Since the initial dust composition is similar for N07 and S12 models, the growth rate is determined largely by the dust size distribution.[3] The characteristic density $n_{{\rm H},i}^{\rm grow}$ where grains rapidly grow decreases with decreasing dust size because the total cross-section of grains per unit dust mass is larger for smaller grains. Although the relation between $n_{{\rm H},i}^{\rm grow}$ and $f_{ij,0}$ is complicated, we find a fitting formula to the density where grains rapidly grow as

$$n_{{\rm H},i}^{\rm grow} = 1.0 \times 10^{12}\,{\rm cm^{-3}} \left(\frac{A_j}{7.1 \times 10^{-10}}\right)^{-2} \left(\frac{f_{ij,0}}{0.1}\right)^{-0.8} \times \left(\frac{r_i^{\rm grow}}{0.01\,\mu{\rm m}}\right)^{2} \left(\frac{a_{i,0}}{1\,\text{Å}}\right)^{-6} \left(\frac{m_{i1}}{m_{\rm H}}\right),$$

which is valid in the range of $f_{ij,0} \lesssim 0.5$. In the above equation, $r_i^{\rm grow} = \langle r^3 \rangle^{1/3}$ is a measure of the average dust size which characterizes the growth rate. Table 4 shows that $r_i^{\rm grow}$ is generally larger for N07 model as we discuss in Section 2.3. Thus, the growth rate is smaller for this model.

The critical metallicity with grain growth depends also on the progenitor mass. For N07M13 model, carbon grains grow because

[3] In our previous paper (Chiaki et al. 2014), where we investigate the effect of grain growth on the formation of the specific star SDSS J102915+172927, employing the part of S12 model, we conclude that the growth rate is almost insensitive to the initial dust models. We in this paper survey a wider range of the initial conditions including N07 model, which predicts larger grain radii than S12 model by about an order of magnitude. Thus, the dependence of the growth rate on the initial dust size becomes apparent.

C > O. The condensation efficiency of carbon increases from the initial value of $f_{\rm C,C,0} = 0.04$–0.38 up to $f_{\rm C,C,*} = 0.13$–0.55 at $n_{\rm H} \sim 10^{12}\,{\rm cm^{-3}}$ with $Z = 10^{-5}\,{\rm Z_\odot}$. Since the carbon abundance is large relative to magnesium, $\log{(A_{\rm C}/A_{\rm Mg})} = 1.24$, the growth of carbon grains enhances gas cooling more efficiently than silicate. The rate of heat transfer between gas and dust becomes proportional to $f_{\rm dep,C,*}S_{\rm C,*} = [2.6$–$30.3] \times 10^4\,{\rm cm^2\,g^{-1}}$, which is larger than the values for silicate grains with the other progenitor masses. Therefore, $Z_{\rm cr,gg}$ is smallest for M13. For N07M13n0 model, MgO grains, which grow at gas density $\log(n_{\rm H,MgO}^{\rm grow}) = 13.8$, further enhance the efficiency of dust cooling. With the other progenitor masses for N07 model, silicate grains become the dominant species. For M20 and M30 models, silicate grow too slowly, at $n_{\rm H} > 10^{15}\,{\rm cm^{-3}}$, to enhance the cooling efficiency for n10 models. In these cases, SiO_2 grains become dominant species for gas cooling. For M25, the contribution of silicate grains to gas cooling becomes comparable to carbon by grain growth for n1 and n10 models. Regardless of the different composition of carbon to silicate, $Z_{\rm cr,gg}$ is within ∼0.2 dex from the value for M20 and M30 models.

For S12 model, the dominant species is changed from carbon to silicate by grain growth for all progenitor masses. Magnetite grains also contribute to gas cooling for M13 and M30 models via their growth at densities $\log(n_{\rm H,Fe_3O_4}^{\rm grow}) = 11.8$–$12.7$ and 12.7–13.8 for the former and latter models, respectively. Fig. 10 shows that the critical metallicity is small for M13 and M20 models. For M13, both magnetite and silicate grow to become dominant. Although this occurs also for M30 models, the mass density of silicate $f_{\rm dep,Sil,*}$ is larger for M13 as shown in Table 4. In addition, both the values $f_{\rm dep,Fe_3O_4,*}$ and $S_{\rm Fe_3O_4,*}$ are larger for M13 than M30: $(f_{\rm dep,Fe_3O_4,*}, S_{\rm Fe_3O_4,*}) = (0.026$–$0.11,\ 18.0$–$40.9)$ for M13, while $(0.004$–$0.070,\ 15.2$–$19.9)$ for M30, where the unit of $S_{\rm Fe_3O_4,*}$ is $10^4\,{\rm cm^2\,g^{-1}}$. For M20, the contribution of carbon grains to gas cooling is still large because of their small size, which further reduces the value $Z_{\rm cr,gg}$.

4 CONCLUSION AND DISCUSSION

We have investigated the conditions for formation of the first low-mass stars in the early Universe in a low-metallicity gas by performing one-zone collapse calculations including grain growth. As the initial abundances of metal and dust and size distribution of grains, we have employed the model of dust formation and destruction in preceding Pop III supernovae presented by N07 and S12. Without grain growth, the critical metallicity is inversely proportional to the initial depletion factor as $Z_{\rm cr,ng} = \mathcal{D}_{\rm cr,ng} f_{\rm dep,0}^{-1}$ with the critical dust-to-gas mass ratio $\mathcal{D}_{\rm cr,ng} = [0.81 : 11.6] \times 10^{-8}$, depending on the supernova models. $\mathcal{D}_{\rm cr,ng}$ is smaller for S12 model than N07 because the mass fractions of carbon and magnetite grains are larger for the former model, and silicon grains, which have less cooling efficiency, account for a considerable mass fraction for N07 model. For S12 model, $\mathcal{D}_{\rm cr,ng}$ is determined mainly by the size of carbon grains, which are dominant coolants for all progenitor masses.

With grain growth, the critical dust-to-gas mass ratio is reduced down to $\mathcal{D}_{\rm cr,gg} = [0.07 : 3.82] \times 10^{-8}$. The corresponding metallicity is around $Z_{\rm cr,gg} \sim 10^{-5}\,{\rm Z_\odot}$, proportional to $f_{\rm dep,0}^{-0.44}$ (equation 12). This dependence on $f_{\rm dep,0}$ becomes milder than the case without grain growth, but the dependence is not completely washed out because of the incomplete accretion of the gas-phase species on to grains. For S12 model, the accretion of magnesium on to silicate grains rapidly occurs. Carbon atoms are depleted on CO molecules before accreted by carbon grains. For N07 model, silicate grains do not completely accrete the gas-phase species because of larger grain radii than S12 model.

It is conceivable that dust evaporation and coagulation by grain–grain collision could reduce the cross-section of collisions between dust grains and gas particles. These processes, however, have little effect on the thermal evolution of the clouds in the region of our interest for the following reasons: first, silicate grains are sublimated at temperature ∼1100 K at high density (Pollack et al. 1994). Gas temperature rises up to such a value only when the dust cooling is not efficient enough to induce cloud fragmentation. Next, grain–grain collision is effective only at densities $n_{\rm H} > 10^{16}(Z/10^{-5}{\rm Z_\odot})^{-2}(T/1000\,{\rm K})^{-1}\,{\rm cm^{-3}}$ (Hirashita & Omukai 2009), where the gas is already optically thick. Therefore, we ignore these effects in this study. We should also mention that, if the sticking coefficient α_i is less than unity, the growth rate of grains is reduced accordingly. This value is still uncertain but considered to be 0.1–1 by various approaches (Leitch-Devlin & Williams 1985; Grassi et al. 2011; Tachibana et al. 2011). We have explicitly tested cases with $\alpha_i = 0.1$ and found that grain growth hardly affects the fragmentation condition: $(Z_{\rm cr}/10^{-5.5}\,{\rm Z_\odot}) = (f_{\rm dep,0}/3.5)^{-0.92}$. In this case, the scaling between $Z_{\rm cr}$ and $\mathcal{D}_{\rm cr}$ is almost the same as expected without grain growth. Let us finally remark that an experimental measurement reveals that the large value of the sticking probability is an order of unity, although this is for Fe grains (Tachibana et al. 2011).

As discussed above, the critical metallicity depends on the composition and size distribution of dust. However, it is not possible to observe directly the properties of dust grains in the formation site of long-lived low-metallicity stars discovered in the Galaxy. Instead, we define the domain of metal abundances where the formation of low-mass stars is favoured. We focus here on carbon-normal stars, which are characterized by [C/Fe] < 0.7 (Beers & Christlieb 2005; Aoki et al. 2007). In such cases, we find that silicate grains are the most important species for the gas cooling for the most cases styled in bold in Tables 3 and 4. We define the range of the critical conditions in terms of silicon abundance from equation (1), setting the metallicity $Z = Z_{\rm cr}$, which are shown by the green and red shaded regions in Fig. 11, for N07 and S12 models, respectively. Our analyses reveal that the dust-induced fragmentation is activated in the region inside the colour-shaded regions. Interestingly, the carbon, oxygen and silicon abundances of the extremely metal-poor (EMP) stars which have so far been observed are located to the right of the colour-shaded region. The formation of the most primitive star ever observed, SDSS J102915+172927 with [Si/H] = −4.3 (Caffau et al. 2011), is favoured by about half of our supernova models even if grain growth does not occur. Furthermore, most of our models can explain the formation of this star by grain growth (Chiaki et al. 2014).

An empirical model for the formation of the first low-mass stars posits that the fine-structure cooling by carbon and oxygen drives the gas fragmentation under the critical discriminant of $D_{\rm trans} = \log{(10^{\rm [C/H]} + 0.9 \times 10^{\rm [O/H]})} > -3.5 \pm 0.2$ (horizontal lines in Fig. 10: e.g. Bromm et al. 2001; Frebel et al. 2005). However, this occurs only at the low densities $n_{\rm H} = 10^2$–$10^3{\rm cm^{-3}}$, where the Jeans mass is ∼ 100 $\rm M_\odot$, which indicates that the low-mass fragments could not be formed by the fine-structure cooling only (Omukai et al. 2005; Schneider et al. 2006). Ji et al. (2014) determine the critical Si abundance above which dust cooling can induce gas fragmentation by equating the gas compressional heating rate and dust cooling rate, assuming that dust consists only of Si-bearing grains. They suggest that the formation of the low-mass stars b–e

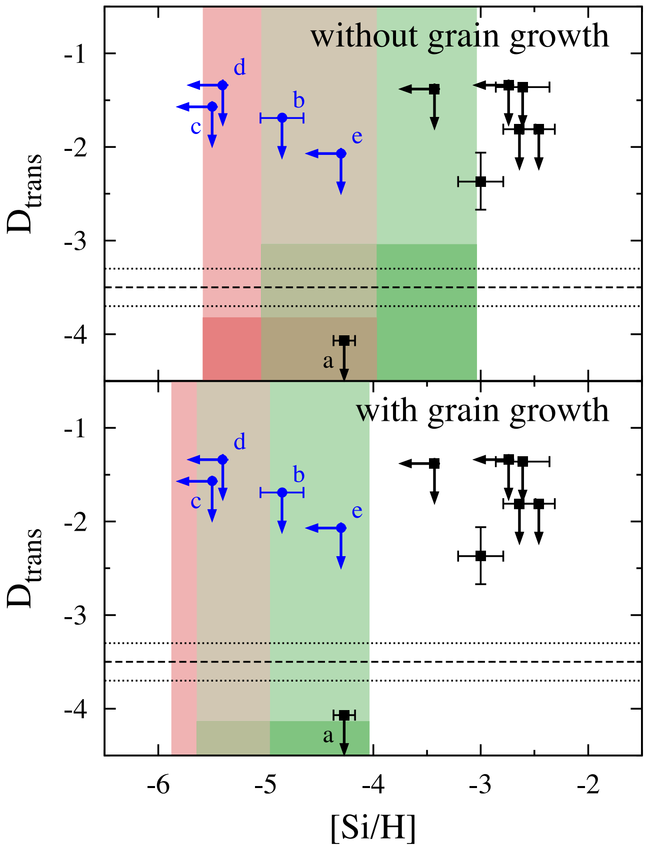

Figure 11. Critical conditions for the formation of low-mass stars plotted on the $D_{\rm trans}$-[Si/H] plane as used by Ji et al. (2014). We show the range of the critical metallicity as the green- and red-coloured regions defined by our one-zone calculations with N07 and S12 models, respectively, without (top panel) and with (bottom) grain growth. The subsets of the regions with darker colours show the range of C and O abundances examined here. We also draw horizontal lines depicting the proposed discriminant, $D_{\rm trans} = -3.5 \pm 0.2$, above which the fine-structure cooling activate the fragmentation (Frebel & Norris 2013). We also plot the abundances of EMP (black squares) and CEMP (blue circles) stars which have so far been observed. The symbols with a–e indicate the elemental abundances of the recently discovered primitive star SDSS J102915+172927 (a: Caffau et al. 2011), and most iron-poor CEMP stars HE0557−4840 (b: Norris et al. 2007), HE0107−5240 (c: Christlieb et al. 2004), HE 1327−2326 (d: Frebel et al. 2008), and SMSS J0313−6708 (e: Keller et al. 2014). The other stars are the carbon-normal main-sequence stars with the intermediate metallicities taken from the SAGA data base (Suda et al. 2008).

in Fig. 10 can not be explained by dust cooling scenario because of the lack of silicon abundance, but can by fine-structure cooling scenario because of more abundant C and O than their discriminant. Although one-zone calculations reveal that subsolar-mass clumps could not be formed in the fine-structure cooling model, Ji et al. (2014) speculate that low-mass star formation could still be possible with the help of some dynamical effects. It is important to note that the contribution of carbon grains, which can reduce the critical Si abundances, is uncertain in their model. The mass ratio of this species is determined for our supernova dust models as 0.003–0.65 and 0.26–0.96 for N07 and S12, respectively. The contribution of the considerable amount of the carbon grains reduces the lower bound of our critical Si abundance down to the value lower than that of the stars b–e even without grain growth. Grain growth can further reduce the critical Si abundance so that a part of N07 models becomes favoured to the formation of these primitive stars.

We in this work focus on the progenitor models which predict the elemental abundance consistent with the carbon-normal stars. The range of $D_{\rm trans}$ is defined from carbon and oxygen abundances of our progenitor models, and is described as the region with dark colour shades in Fig. 11. The carbon-enhanced iron-poor stars with [C/Fe] > 0.7 should lie in the upper regime than the dark-coloured region, where our model fails to reproduce the properties of these stars. To explain the formation path of the carbon-enhanced metal-poor (CEMP) stars, we would need to consider additional processes such as the metal pollution by the faint supernovae (Umeda & Nomoto 2002), and the elemental transfer from companion stars (Suda et al. 2004). In Marassi et al. (2014), we discuss the formation of the most primitive carbon-enhanced star, SMSS J0313−6708, assuming that the parent cloud of this star is polluted with metal and dust by the preceding faint supernova explosions. In such cases, the carbon is dominant grain species, and the grain growth is not important because these grains can hardly accrete carbon atoms because of depletion into CO molecules. Therefore, the fragmentation property of the gas clouds is determined by the initial dust-to-gas mass ratio. Our further comprehensive studies for the faint supernova models, as well as our present work on carbon-normal stars, can reveal the entire formation processes of the various categories of long-lived metal-poor stars.

ACKNOWLEDGEMENTS

We thank Simone Bianchi for his kind contribution. GC is supported by Research Fellowships of the Japan Society for the Promotion of Science (JSPS) for Young Scientists. This work is supported by World Premier International Research Center Initiative (WPI Initiative), MEXT, Japan and in part by Grant-in-Aid for Scientific Research from the JSPS Promotion of Science (22684004, 23224004, 23540324, 25287040, 25287050, and 26400223). A part of calculations is performed with COMA at Center for Computational Sciences in University of Tsukuba. The research leading to these results has received funding from the European Research Council under the European Union's Seventh Framework Programme (FP/2007-2013)/ERC Grant Agreement n. 306476. ML acknowledges the following funding sources: PRIN INAF 2009 'Supernova Variety and Nucleosynthesis Yields', and PRIN MIUR 2010–2011, project 'The Chemical and dynamical Evolution of the Milky Way and Local Group Galaxies', prot. 2010LY5N2T.

REFERENCES

Abel T., Bryan G. L., Norman M. L., 2002, Science, 295, 93
Aoki W., Beers T. C., Christlieb N., Norris J. E., Ryan S. G., Tsangarides S., 2007, ApJ, 655, 492
Beers T. C., Christlieb N., 2005, ARA&A, 43, 531
Bianchi S., Schneider R., 2007, MNRAS, 378, 973
Bromm V., Loeb A., 2003, Nature, 425, 812
Bromm V., Ferrara A., Coppi P. S., Larson R. B., 2001, MNRAS, 328, 969
Caffau E. et al., 2011, Nature, 477, 67
Cazaux S., Tielens A. G. G. M., 2002, ApJ, 575, L29
Chiaki G., Nozawa T., Yoshida N., 2013, ApJ, 765, L3
Chiaki G., Schneider R., Nozawa T., Omukai K., Limongi M., Yoshida N., Chieffi A., 2014, MNRAS, 439, 3121
Christlieb N., Gustafsson B., Korn A. J., Barklem P. S., Beers T. C., Bessell M. S., Karlsson T., Mizuno-Wiedner M., 2004, ApJ, 603, 708

De Cia A., Ledoux C., Savaglio S., Schady P., Vreeswijk P. M., 2013, A&A, 560, 88
Frebel A., Norris J. E., 2013, Planets, Stars and Stellar Systems. Vol. 5, Galactic Structure and Stellar Populations. Springer Science+Business Media, Dordrecht, p. 55
Frebel A. et al., 2005, Nature, 434, 871
Frebel A., Johnson J. L., Bromm V., 2007, MNRAS, 380, L40
Frebel A., Collet R., Eriksson K., Christlieb N., Aoki W., 2008, ApJ, 684, 588
Grassi T., Krstic P., Merlin E., Buonomo U., Piovan L., Chiosi C., 2011, A&A, 533, A123
Hartquist T. W., Dalgarno A., Oppenheimer M., 1980, ApJ, 236, 182
Hirano S., Hosokawa T., Yoshida N., Umeda H., Omukai K., Chiaki G., Yorke H. W., 2014, ApJ, 781, 60
Hirashita H., Omukai K., 2009, MNRAS, 399, 1795
Hosokawa T., Omukai K., Yoshida N., Yorke H. W., 2011, Science, 334, 1250
Inutsuka S.-I., Miyama S. M., 1997, ApJ, 480, 681
Ji A. P., Frebel A., Bromm V., 2014, ApJ, 782, 95
Keller S. C. et al., 2014, Nature, 506, 463
Kitayama T., Yoshida N., Susa H., Umemura M., 2004, ApJ, 613, 631
Kroupa P., 2002, Science, 295, 82
Langer W. D., Glassgold A. E., 1990, ApJ, 352, 123
Larson R. B., 1985, MNRAS, 214, 379
Leitch-Devlin M. A., Williams D. A., 1985, MNRAS, 213, 295
Limongi M., Chieffi A., 2012, ApJS, 199, 38
Marassi S., Chiaki G., Schneider R., Limongi M., Omukai K., Nozawa T., Chieffi A., Yoshida N., 2014, ApJ, 794, 100
Mayer M., Duschl W. J., 2005, MNRAS, 358, 614
Molaro P., Bonifacio P., Centurión M., D'Odorico S., Vladilo G., Santin P., Di Marcantonio P., 2000, ApJ, 541, 54
Norris J. E., Christlieb N., Korn A. J., Eriksson K., Bessell M. S., Beers T. C., Wisotzki L., Reimers D., 2007, ApJ, 670, 774
Nozawa T., Kozasa T., Umeda H., Maeda K., Nomoto K., 2003, ApJ, 598, 785
Nozawa T., Kozasa T., Habe A., Dwek E., Umeda H., Tominaga N., Maeda K., Nomoto K., 2007, ApJ, 666, 955 (N07)
Nozawa T. et al., 2008, ApJ, 684, 1343
Nozawa T., Kozasa T., Nomoto K., 2012, ApJ, 756, L35
Omukai K., 2000, ApJ, 534, 809
Omukai K., Palla F., 2003, ApJ, 589, 677
Omukai K., Tsuribe T., Schneider R., Ferrara A., 2005, ApJ, 626, 627
Omukai K., Hosokawa T., Yoshida N., 2010, ApJ, 722, 1793
Pollack J. B., Hollenbach D., Beckwith S., Simonelli D. P., Roush T., Fong W., 1994, ApJ, 421, 615
Santoro F., Shull J. M., 2006, ApJ, 643, 26
Schneider R., Omukai K., 2010, MNRAS, 402, 429
Schneider R., Ferrara A., Salvaterra R., Omukai K., Bromm V., 2003, Nature, 422, 869
Schneider R., Omukai K., Inoue A. K., Ferrara A., 2006, MNRAS, 369, 1437
Schneider R., Omukai K., Bianchi S., Valiante R., 2012a, MNRAS, 419, 1566 (S12)
Schneider R., Omukai K., Limongi M., Ferrara A., Salvaterra R., Chieffi A., Bianchi S., 2012b, MNRAS, 423, L60
Silvia D. W., Smith B. D., Shull J. M., 2010, ApJ, 715, 1575
Silvia D. W., Smith B. D., Shull J. M., 2012, ApJ, 748, 12
Suda T., Aikawa M., Machida M. N., Fujimoto M. Y., Iben I., Jr, 2004, ApJ, 611, 476
Suda T. et al., 2008, PASJ, 60, 1159
Susa H., Hasegawa K., Tominaga N., 2014, ApJ, 792, 32
Tachibana S., Nagahara H., Ozawa K., Ikeda Y., Nomura R., Tatsumi K., Joh Y., 2011, ApJ, 736, 16
Todini P., Ferrara A., 2001, MNRAS, 325, 726
Umeda H., Nomoto K., 2002, ApJ, 565, 385
Whalen D., Abel T., Norman M. L., 2004, ApJ, 610, 14
Yoshida N., Omukai K., Hernquist L., Abel T., 2006, ApJ, 652, 6

This paper has been typeset from a TEX/LATEX file prepared by the author.